CRYSTAL GROWTH & DESIGN

pubs.acs.org/crystal

Article

Liquid Phase Epitaxy Growth of Tm^{3+} and Yb^{3+} Doped $MgWO_4$ Crystalline Thin-Films

Ghassen Zin Elabedine, Rosa Maria Solé, Magdalena Aguiló, Francesc Díaz, Weidong Chen, Valentin Petrov, and Xavier Mateos*

Cite This: *Cryst. Growth Des.* 2025, 25, 9069–9077

Read Online

ACCESS | Metrics & More | Article Recommendations

ABSTRACT: Single-crystalline layers of $MgWO_4$ doped with Tm^{3+} and Yb^{3+} were successfully grown by the liquid phase epitaxy (LPE) method on (010) oriented $MgWO_4$ substrates using $K_2W_2O_7$ as a solvent, for the first time. These layers were transparent and free of cracks, with the Tm:$MgWO_4$ layer reaching a thickness of up to 300 μm and the Yb:$MgWO_4$ layer up to 90 μm. Structural and morphological characterizations were performed to evaluate the quality of both types of doped layers. High-Resolution X-ray Diffraction (HRXRD) rocking curves revealed full width at half-maximum (FWHM) values of 115 arcsec for the Tm^{3+}-doped layer and 140 arcsec for the Yb^{3+}-doped layer, in close agreement with their respective substrates reflecting a good crystal quality and a highly ordered lattice structure. Environmental Scanning Electron Microscopy (ESEM) analysis showed well-defined and continuous interfaces for both samples, and electron probe microanalysis (EPMA) measurements confirmed that the dopants remained confined within the epitaxial regions. The lattice mismatch between the layers and the substrate was calculated and found to be very low. These results demonstrate the capability of the LPE technique to produce relatively thick and optically transparent $MgWO_4$ epitaxial layers doped with different rare-earth ions. The interface between the substrate and the epitaxial layer was very sharp. Based on the known spectroscopic properties of Tm^{3+}- and Yb^{3+}-doped $MgWO_4$ bulk crystals, these films represent promising candidates for applications in thin disk lasers with simplified pump geometry.

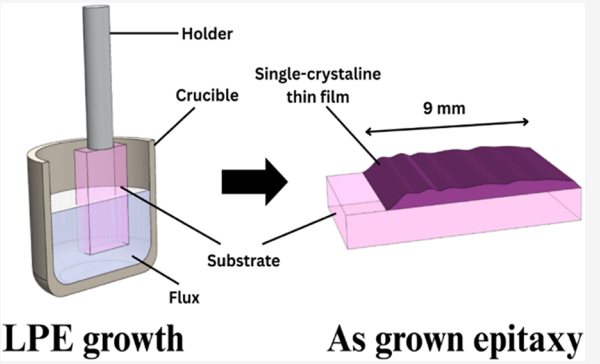

1. INTRODUCTION

Liquid Phase Epitaxy (LPE) is a widely used method for fabricating single-crystalline layers with excellent optical properties.[1,2] This process involves growing a uniform film, typically a few micrometers thick, on a flat, polished crystalline substrate along a specified crystallographic direction. The work by Tien et al.[3] demonstrated the first LPE optical application using 2.4 μm thick gallium and iron garnet films. Following this breakthrough, crystalline layers of different symmetry, such as monoclinic $KLu(WO_4)_2$,[4] cubic $Y_3Al_5O_{12}$ (YAG),[5] and tetragonal $LiYF_4$,[6] have been successfully grown using the LPE technique.

The incorporation of trivalent rare-earth ions (RE^{3+}) into these thin films has gained significant interest for laser applications. In waveguide lasers, the introduction of RE^{3+} ions can create a positive refractive index contrast with the substrate, enabling light confinement through total internal reflection and waveguiding effect. Examples of such waveguide laser operation include Tm^{3+}-doped $KY(WO_4)_2$[7] and Nd^{3+} doped YAG[8] thin films. Moreover, these epitaxial thin films offer significant potential as replacements for traditional thin-disk laser technology, which typically relies on laser elements a few hundred micrometers thick. The thin-disk concept, widely adopted in various commercial lasers, spans applications from medium-power systems to multi-kW lasers, including both continuous-wave (CW) and pulsed lasers, with pulse durations ranging from femtoseconds to nanoseconds. The fundamental principle of thin-disk lasers lies in utilizing a thin, disk-shaped active medium that is efficiently longitudinally cooled via one of the flat surfaces, providing a high surface-to-volume ratio and excellent thermal management. For optimal performance in thin-disk lasers, either a high absorption cross-section of the RE^{3+} ions or a high doping concentration is crucial. Successful thin-disk lasers based on LPE-doped films have been reported with Ho^{3+},[9] Yb^{3+},[10] and Tm^{3+}[11] ions, showing their potential for high-performance laser applications by simplifying the multipass pump geometry compared to the well-known YAG-

Received: June 27, 2025
Revised: October 5, 2025
Accepted: October 7, 2025
Published: October 15, 2025

https://doi.org/10.1021/acs.cgd.5c00954
Cryst. Growth Des. 2025, 25, 9069–9077

based thin-disk lasers. The above-mentioned monoclinic double tungstates, e.g., $KY(WO_4)_2$ show the highest transition cross sections for selected polarizations among all crystalline hosts and simultaneously permit the highest doping levels but power scaling is limited by the moderate thermal conductivity of ~3 W/m.K.

Magnesium monotungstate ($MgWO_4$) has recently emerged as a promising laser host material for doping with RE^{3+}. This crystal is also monoclinic (space group $P2/c$, point group $2/m$) and exhibits similarly strong optical anisotropy but its thermal conductivity of ~8.7 W/m.K[12] is nearly three times higher compared to the monoclinic double tungstates. Tm^{3+} and Yb^{3+} doped $MgWO_4$ shows intense and strongly polarized absorption and emission spectral bands, essential for linearly polarized laser emission.[13,14] The RE^{3+} dopant ions substitute for the divalent Mg^{2+} ions at C_2 sites in the $MgWO_4$ lattice. The difference in ionic radii between Mg^{2+} and RE^{3+} ions induces a distortion in the crystal field, leading to significant Stark splitting of the ground states, which results in broad emission bands and low-threshold laser behavior.[13,15] On the negative side, this leads to low segregation coefficients and high doping levels are difficult to achieve.

Laser performance of $MgWO_4$ has been already demonstrated with few RE^{3+} dopants, yielding highly promising results. Specifically, a Tm^{3+}:$MgWO_4$ laser delivered a CW output of 3.09 W at 2022−2034 nm with a slope efficiency of 50%, indicating a potential for power-scalable, multi-Watt, diode-pumped operation near 2 μm.[16] Additionally, broad wavelength tuning across 1897−2062 nm and operation up to 2093 nm through the vibronic mechanism (electron−phonon coupling) have been achieved with such lasers.[15] Notably, the first sub-100 fs pulses from a mode-locked 2 μm solid-state laser were generated using a Tm^{3+}:$MgWO_4$ crystal.[17] Another significant achievement was the development of a diode-pumped Yb^{3+}:$MgWO_4$ laser, which delivered 18.2 W output at ~1056 nm with a high slope efficiency of 89% and linearly polarized output,[13] setting a record for Yb^{3+}-doped tungstate laser crystals. Recently, a diode-pumped Yb^{3+}:$MgWO_4$ laser delivered 32 fs pulses via Kerr-lens mode-locking.[18]

Despite the impressive progress in LPE growth of crystalline thin films for optical applications and the promising results with RE^{3+}-doped $MgWO_4$ bulk crystals, growth of such monotungstate crystals via LPE has not been reported, yet. In the present work, we demonstrate for the first time LPE growth of Tm^{3+}:$MgWO_4$ and Yb^{3+}:$MgWO_4$ crystalline layers. The morphological and structural studies confirm the high quality of the doped layers making them attractive for potential use in thin-disk lasers, based on the known spectroscopic performance of their bulk counterparts.

2. EXPERIMENTAL SECTION

2.1. Single Crystal Growth of Undoped Bulk $MgWO_4$ for Use as Substrates. Undoped $MgWO_4$ crystals were successfully grown using the top-seeded solution growth (TSSG) method. The experimental setup included a vertical cylindrical furnace and cylindrical Pt crucibles with a diameter of 50 mm. A solution, weighing approximately 150 g, was prepared with a composition ratio of $MgWO_4/K_2W_2O_7$ = 25/75. The solute reagents used were MgO and WO_3, while K_2CO_3 and WO_3 were employed to form the solvent. $K_2W_2O_7$ was selected as the solvent due to its low melting point (~620 °C/cm) and its high tungsten content, which contributes to reduce the solution viscosity significantly increasing the growth rate.

After placing the Pt crucible into the furnace, the solution was homogenized by maintaining the temperature at 50 °C above the expected saturation temperature (T_{SA}). The axial thermal gradient in the solution was kept at 1.4 °C/cm. The precise T_{SA} was determined through repeated seeding experiments using a $\boldsymbol{b}$ oriented $MgWO_4$ seed in contact with the surface of the solution. Crystal growth commenced with a gradual reduction of the temperature at a rate of 0.12 °C/h, down to 40 °C below T_{SA}, while the seed crystal rotated at 40 rpm.

Upon completion of the growth, the crystal was carefully extracted from the solution and positioned just above the liquid surface, followed by a controlled cooling of the furnace to room temperature at a rate of 40 °C/h. The resulting crystal exhibited high optical quality with a slightly pink hue. Its dimensions were 11.3 mm × 10.6 mm × 14.9 mm along the $\boldsymbol{a}^*$ × $\boldsymbol{b}$ × $\boldsymbol{c}$ crystallographic directions, where we adopted the $a < c$ convention for the $P2/c$ space group ($\boldsymbol{b}$: monoclinic axis and $\beta > 90°$: monoclinic angle in the right-handed abc frame), with a final weight of 6.63 g. Figure 1 depicts the $MgWO_4$ single crystal obtained under the above growth conditions. Subsequently, few further crystals with very similar dimensions and quality were also grown.

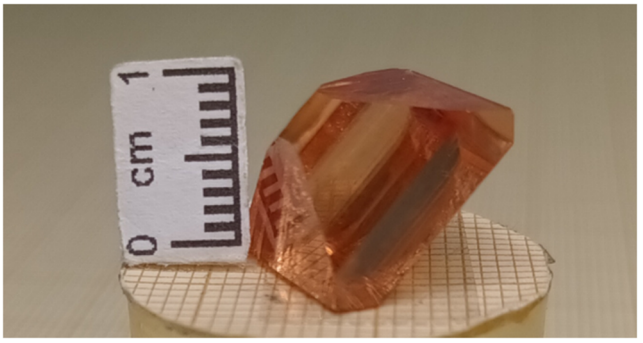

Figure 1. Photograph of the as-grown $MgWO_4$ crystal before being sliced for substrates.

2.2. Liquid-Phase Epitaxial Growth. The LPE growth experiments were carried out using a custom-designed vertical furnace, optimized for a wide zone of uniform temperature distribution to effectively minimize thermal gradients within the solution. The furnace is isolated from external thermal interference through multiple layers of refractory brick shells. Heating is supplied by a Kanthal resistance coil, which is arranged around an inner alumina tube positioned along the central axis of the furnace. The substrate holder, made of alumina, is an adjustable rod that can be moved vertically to immerse the substrate into the solution using a handle pull mechanism. A DC motor, connected to a power supply, drives the rotation of the rod, see Figure 2 for a detailed illustration.

The solution was prepared by combining approximately 80 g of reagents in a cylindrical Pt crucible 30 mm in diameter. The solute to solvent ratio was the same as for the bulk crystal growth, i.e., 25/75, using the same reagents with the addition of Tm_2O_3 and Yb_2O_3 for substitution, to reach molar doping levels of 10% and 20% with respect to MgO, respectively.

Once homogeneity of the solution was established, T_{SA} was precisely determined in each experimental run. To optimize the epitaxial growth process, the kinetics of seed crystal growth and dissolution were investigated at various temperatures in close proximity to T_{SA}.

Figure 3 provides an overview of the fabrication process for single-crystalline Tm^{3+}:$MgWO_4$ and Yb^{3+}:$MgWO_4$ layers grown on $MgWO_4$ substrates. Planar substrates were prepared by slicing 1.5 mm thick sections from a single crystal using a diamond saw. After that, the substrates were double-side polished to optical quality. The polished faces were perpendicular to the $\boldsymbol{b}$-axis and the plates were immersed in the solution with the $\boldsymbol{c}$-axis perpendicular to the solution's surface. Before being placed in the furnace, the substrates underwent a thorough cleaning process, including sequential immersion in a 1:1

https://doi.org/10.1021/acs.cgd.5c00954
Cryst. Growth Des. 2025, 25, 9069−9077

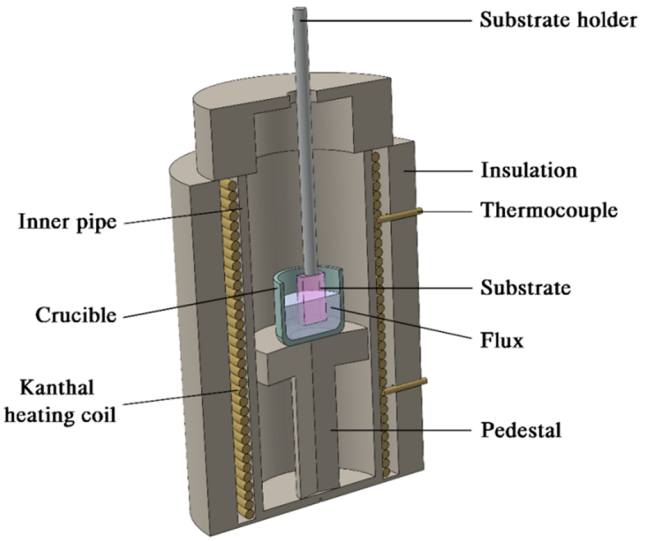

Figure 2. Scheme of the experimental setup for the Liquid Phase Epitaxy (LPE) growth of Yb^{3+}:$MgWO_4$ and Tm^{3+}:$MgWO_4$ layers on undoped $MgWO_4$ substrates.

HNO_3/H_2O solution (5 min), distilled water (5 min), acetone (5 min), and ethanol (5 min).

The substrates were initially introduced slowly into the furnace and positioned near the solution's surface for about 30 min to reach thermal equilibrium. Following this, they were immersed into the solution at 1 °C above the saturation temperature to promote the dissolution of the outer substrate layer, with the substrates held at this temperature for 3 min. Subsequently, the temperature was reduced back to T_{SA} to initiate the epitaxial growth process. The temperature was then gradually lowered at a rate of 0.2 °C/h, eventually reaching 4 °C below the saturation temperature. Throughout the process, the crystal was rotated at a constant speed of 15 rpm.

To avoid cracking due to thermal shock caused by differences in thermal expansion coefficients between the epitaxial layer and the substrate, and considering the anisotropy of $MgWO_4$, the crystal was carefully extracted from the solution and gradually removed from the furnace. The epitaxial growth took place also on the remaining unpolished faces of the substrates.

The actual RE^{3+} doping levels in the epitaxial layers were determined by electron probe microanalysis using wavelength-dispersive spectroscopy (EPMA-WDS) on a Cameca Camebax SX-100 analyzer. Quantitative measurements revealed that the concentration of Tm^{3+} ions in the crystal was 0.40 at%, corresponding to a segregation coefficient (K_{Tm}) of 0.040, calculated as the ratio of the dopant concentration in the crystal to that in the melt or solution phase ($K_{Tm} = C_{crystal}/C_{solution}$). Similarly, the measured Yb^{3+} doping level was 0.62 at%, yielding a segregation coefficient (K_{Yb}) of 0.031. These values are notably lower than those reported for bulk $MgWO_4$ crystals grown by TSSG method in our previous work,[19] where K_{Tm} = 0.078 and K_{Yb} = 0.111 were obtained. In the case of Tm^{3+}, both the bulk and epitaxial samples were grown from melts containing 10 at% dopant, while for Yb^{3+}, the initial concentration in the LPE melt was increased to 20 at%, compared to 10 at% used in bulk growth. Despite this higher starting concentration, the actual Yb incorporation in the epitaxial layer was lower, reflecting a significantly reduced segregation efficiency.

This discrepancy is primarily attributed to the different growth environments and incorporation dynamics between LPE and TSSG. In bulk growth, the larger solution volume, longer growth durations, and slower interface kinetics allow more time for dopant ions to diffuse toward the growing interface and be effectively incorporated into the crystal lattice. In contrast, LPE typically operates with a smaller solution volume, shorter growth times, and a thin, localized growth interface, where atoms must integrate rapidly into the crystal structure. These faster interface kinetics mean that dopant ions have less time to incorporate, and the process becomes more sensitive to factors such as charge compensation requirements and surface segregation effects. These limitations become especially significant at higher doping concentrations, as in the 20 at% Yb^{3+} case, where the crystal's capacity to incorporate excess dopants is limited. Together, these factors explain why the segregation coefficients in LPE-grown layers are lower compared to those in bulk-grown crystals.

2.3. Characterization Methods. The crystallinity and the growth direction of the films were confirmed by X-ray diffraction (XRD) measurements in the θ-θ Bragg–Brentano configuration. The measurements were performed using a Bruker-AXS D8-Advance diffractometer and Cu Kα radiation (λ = 0.15406 nm) at 40 kV and 30 mA, for room temperature conditions (293 K). The scan rate was 3 s per step, with a step size of 0.05° over a 2θ range of 10° to 70°.

To further evaluate the crystalline quality of the epitaxial layers, rocking curve (RC) measurements of the (030) reflection were performed on both Tm^{3+}:$MgWO_4$ and Yb^{3+}:$MgWO_4$ films using the

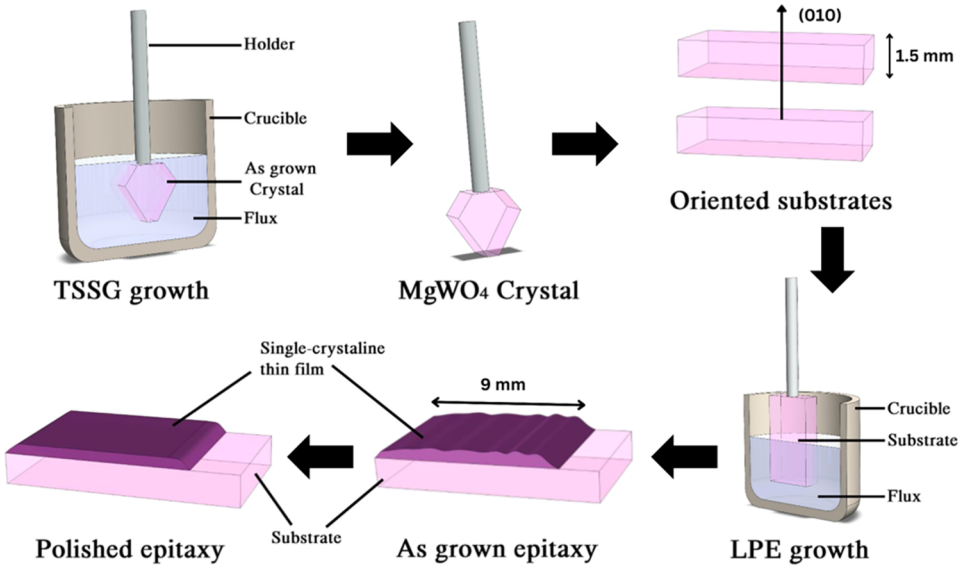

Figure 3. Fabrication process of single-crystalline Tm^{3+}:$MgWO_4$ and Yb^{3+}:$MgWO_4$ thin films on ***b***-oriented undoped $MgWO_4$ substrates.

https://doi.org/10.1021/acs.cgd.5c00954
Cryst. Growth Des. 2025, 25, 9069−9077

same X-ray system. The ω-scan was recorded over a ± 1.2° range, using 120 frames with a step size of 0.02 ° and an exposure time of 10 s per frame. The RC profiles were extracted by integrating the central region of each frame using the GADDS (Bruker AXS) software.

The surface morphology of the as-grown films was studied employing a confocal microscope in reflection mode and the layer topography was studied in the interferometric mode.

The substrate/epitaxial layer interface was observed for a polished end-facet of the epitaxy using Environmental Scanning Electron Microscopy (ESEM) in backscattered mode, while electron probe microanalysis was used to study the composition change in the interface.

3. RESULTS AND DISCUSSION

3.1. Lattice Mismatch. The lattice mismatch between the substrate and the epitaxial layer is a critical factor affecting the quality of the substrate/layer interface. Significant mismatches can introduce stress at the interface, potentially leading to crack formation and propagation within the layer.[20] Considering the differences in lattice constants between $MgWO_4$ and Tm^{3+}- or Yb^{3+}-doped $MgWO_4$, obtained in our previous work,[19] we calculated the mismatch for various crystallographic faces for both Tm^{3+} and Yb^{3+} doped layers using the following expression

$$f_{(hkl)} = (S_{(hkl)}(\text{subst}) - S_{(hkl)}(\text{layer}))/S_{(hkl)}(\text{subst})$$

where $S_{(hkl)}(\text{subst})$ and $S_{(hkl)}(\text{layer})$ represent the areas derived from the (hkl) periodicity vectors of the substrate and the epitaxial layer, respectively. The mismatches calculated for different faces and doping ions are summarized in Table 1.

Table 1. Mismatch between $MgWO_4$ Substrates and Tm^{3+}/Yb^{3+}-Doped $MgWO_4$ Layers

epitaxial layer	$f_{(100)}$	$f_{(010)}$	$f_{(001)}$
$Mg_{0.9}Tm_{0.1}WO_4$	−0.00082	−0.0019	−0.00113
$Mg_{0.9}Yb_{0.2}WO_4$	−0.00100	−0.0024	−0.00154

Analysis of the data in Table 1 reveals that the mismatches are particularly low along the (100) face. Overall, the mismatches across all crystallographic directions are also very low, suggesting favorable conditions for epitaxial growth on $MgWO_4$ substrates.

The (010) mismatch for the Tm^{3+}:$MgWO_4$ layer is −0.0019, while that of the Yb^{3+}:$MgWO_4$ layer is slightly higher at −0.0024. Both values fall within low mismatch conditions, confirming excellent lattice compatibility between the doped layers and the $MgWO_4$ substrate.

The mismatch values of Yb^{3+}:$MgWO_4$ are comparable to or lower than those reported in other RE^{3+} monoclinic double-tungstate systems. For example, compared to the (010) mismatch in the $KY_{0.8}Yb_{0.2}(WO_4)_2/KY(WO_4)_2$ system (−0.00107),[21] and in the $KLu_{0.78}Yb_{0.22}(WO_4)_2/KLu(WO_4)_2$ system (−0.003125),[4] the mismatch for Yb^{3+}:$MgWO_4$ lies between these two widely studied systems. This positions $MgWO_4$ as a structurally compatible host, particularly given that both $KY(WO_4)_2$ and $KLu(WO_4)_2$ have been successfully used for high-quality epitaxial growth and laser applications. The similarly low mismatch in $MgWO_4$—for both Tm^{3+} and Yb^{3+} dopants—highlights its suitability for the development of structurally coherent and optically promising epitaxial films.

3.2. Structure of the Layer. The structure and orientation of the Yb^{3+}-doped and Tm^{3+}-doped layers were verified using XRD, as shown in Figure 4(a). The XRD patterns revealed reflections corresponding to the (010), (020), (030), and (040) crystallographic planes of monoclinic $MgWO_4$, indicated by the Miller indices (hkl). These observations confirm the high crystallinity degree and phase purity of the grown layer and the orientation of its normal along the[10] axis, consistent with the substrate. The diffraction peaks match well with the PDF card #73−0562 for undoped $MgWO_4$.

The $MgWO_4$ crystal symmetry is monoclinic (space group C_{2h}^4—$P2/c$, No. 13). Similar to other monoclinic divalent-metal monotungstates, $MgWO_4$ adopts a wolframite-type structure ([(Fe,Mn)WO_4]). In this structure, Mg^{2+} cations, located at 2f Wyckoff positions, are VI-fold O^{2-} coordinated, forming distorted [MgO_6] octahedra. Similarly, W^{6+} cations, positioned at 2e Wyckoff sites, are also found in distorted octahedra. The $MgWO_4$ structure comprises alternating zigzag chains of edge-sharing [MgO_6] and [WO_6] polyhedra along the c-axis, as illustrated in Figure 4(b).

RE^{3+} dopant ions are expected to substitute for Mg^{2+} ions due to their similar coordination environments, despite the significant difference in ionic radii (R_{Mg} = 0.72 Å, R_{Tm} = 0.88 Å, R_{Yb} = 0.868 Å for a coordination number of VI).[22] However, the trivalent nature of RE^{3+} compared to the divalent Mg^{2+} introduces a charge imbalance that must be compensated, often through the formation of M^{2+} vacancies or the incorporation of monovalent cations (e.g., Na^+, K^+ from the flux in the case of $MgWO_4$). This substitution leads to additional distortion in the [MgO_6]/[REO_6] polyhedra,

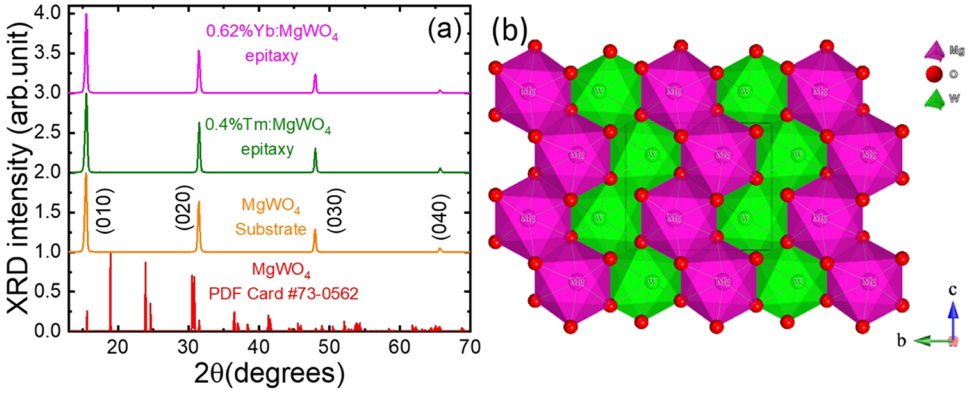

Figure 4. (a) X-ray diffraction of the Tm^{3+} doped and Yb^{3+} doped $MgWO_4$ films and the substrate, and (b) crystal structure in projection to the ***b*-*c*** plane.

https://doi.org/10.1021/acs.cgd.5c00954
Cryst. Growth Des. 2025, 25, 9069−9077

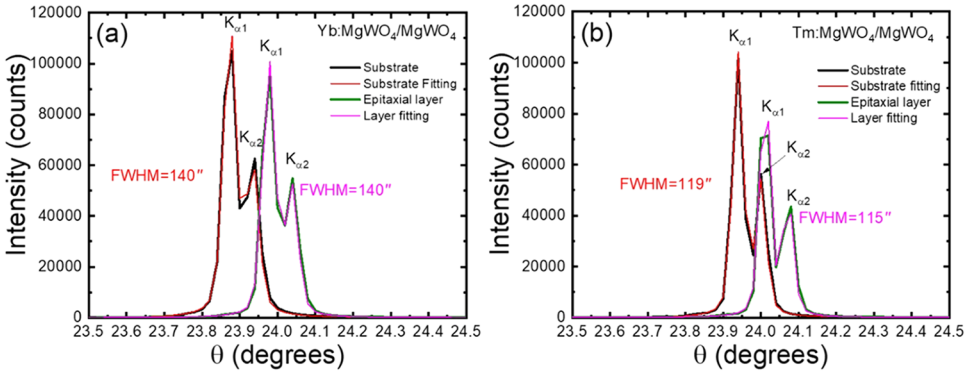

Figure 5. High-resolution X-ray rocking curves (HRXRD) of the (030) reflection for (a) 0.62%Yb^{3+}:$MgWO_4$ and (b) 0.4%Tm^{3+}:$MgWO_4$ epitaxial layers grown on $MgWO_4$ substrates.

enhancing crystal-field distortions for the RE^{3+} ions and resulting in significant Stark splitting and broad spectral bands.[13,15]

To characterize the epitaxial layer quality, high-resolution X-ray diffraction (HRXRD) measurements were performed on the (030) reflection of each layer and their respective substrates, as shown in Figure 5. The spectra exhibit two distinct peaks corresponding to the epitaxial layers and the substrates, each split into $K_{\alpha1}$ and $K_{\alpha2}$ components due to the X-ray source; we fitted both peaks to pseudo-Voigt functions.

From the figure, the rocking curves exhibit symmetrical profiles without the presence of spurious peaks, indicating high structural uniformity and the absence of significant crystallographic defects or impurity phases. The full width at half-maximum (FWHM) values further support the structural quality assessment: for the 0.4%Tm:$MgWO_4$ epitaxial layer. The FWHM was 115 arcsec, closely matching that of its substrate (119 arcsec). This narrow width reflects excellent crystalline quality and minimal lattice distortion in both the layer and substrate, pointing to a well-optimized growth process and strong lattice compatibility. In comparison, the 0.62%Yb:$MgWO_4$ epitaxial layer exhibited a FWHM of 140 arcsec, consistent with that of its substrate, also 140 arcsec. These values still reflect good crystal quality and a highly ordered lattice structure. The close agreement between the substrate and the epilayer suggests that the structural quality of the film is strongly influenced by the substrate's characteristics. Although slightly broader than the Tm-doped system, the Yb-doped film rocking curve remains narrow, and its slightly reduced sharpness compared to the Tm-doped one is likely related to the higher initial dopant concentration (20% Yb), which may introduce moderate lattice strain and point defects. Moreover, the substrate initial quality may impose a practical upper limit on the achievable perfection in the overgrown film. Overall, both systems demonstrate successful epitaxial growth, with the 0.4%Tm-doped sample achieving slightly superior structural quality due to more favorable substrate properties and optimized doping levels.

3.3. Morphology of the Epitaxies. Figure 6 presents an image of an as-grown Yb^{3+}:$MgWO_4$ epitaxial layer on a ***b***-oriented $MgWO_4$ substrate. The epitaxial layer covered all sides of the immersed substrate, with a clearly visible meniscus indicating the boundary between the immersed and non-immersed regions. The total immersed length was approximately 9 mm. Morphological assessment using a confocal microscope revealed an average layer thickness of 90 μm on both (010) substrate faces, with consistent thickness across the

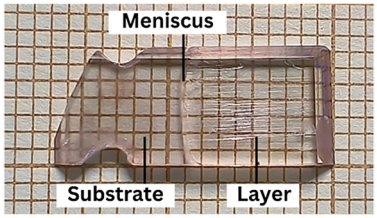

Figure 6. Photograph of an as-grown Yb^{3+}:$MgWO_4$ layer on the $MgWO_4$ substrate showing the (010) plane.

examined regions. The layer appeared optically transparent, smooth, and free of cracks, suggesting stable growth conditions and good lattice compatibility with the substrate.

Notably, only faint growth lines were observed on the (010) surfaces, as shown in Figure 6. These lines likely reflect step-flow growth features formed during the LPE process, which can occur under conditions of modest supersaturation and slow growth advancement. The absence of cracks and the uniform coverage over the substrate surfaces, indicate stable growth and minimal thermal mismatch stress, which are essential for high-quality functional epitaxial films.

Figure 7(a) shows a confocal optical microscope image of the top surface of an as-grown Yb^{3+}:$MgWO_4$ epitaxial layer, captured at 20× magnification. The visible parallel lines correspond to the surface features previously seen in the as-grown sample (Figure 6), suggesting they are inherent to the growth process. To further characterize the surface morphology, a three-dimensional (3D) topography map was obtained using the same microscope, from which a 2D transverse surface profile was extracted along the A−B direction, as illustrated in Figure 7(b).

The analysis revealed a root-mean-square (rms) surface roughness of approximately 0.62 μm, with a periodic structure composed of alternating "hills" and "valleys" spanning a few micrometres in height. These undulating surface features likely originate from step-flow or terrace-based growth mechanisms during the LPE process. Overall, the surface morphology is typical of thick epitaxial layers grown from solution and reflects a well-formed but moderately textured growth front.

Figure 8 shows the analysis of the substrate/layer interface of the Yb^{3+}:$MgWO_4$ epitaxial structure using environmental scanning electron microscopy (ESEM) in backscattered electron mode. For this purpose, one of the edge facets was carefully polished to reveal the cross-sectional structure. The interface appears clean, sharp, and linear, with no visible

https://doi.org/10.1021/acs.cgd.5c00954
Cryst. Growth Des. 2025, 25, 9069−9077

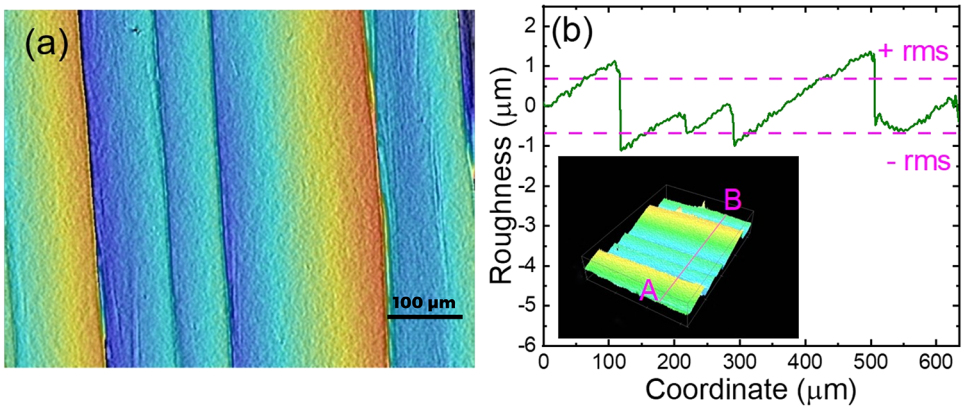

Figure 7. (a) Top view of the raw surface of the LPE-grown Yb: $MgWO_4$ observed by interferometry; (b) Surface roughness plot obtained using a confocal optical microscope. Dash lines indicate the range of root-mean-square (rms) deviation of the roughness, *inset*—the corresponding topography map, A-B *line*—the analyzed direction. Reflection mode, λ = 405 nm.

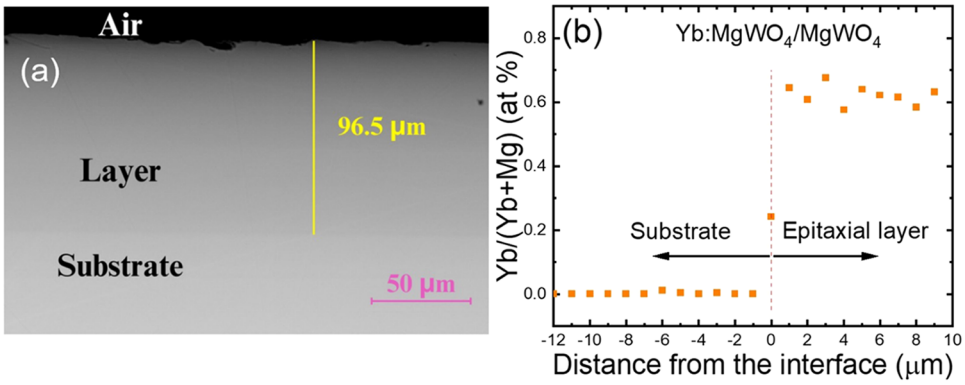

Figure 8. (a) ESEM image in backscattered mode of the polished edge of an Yb:$MgWO_4$/$MgWO_4$ epitaxy showing the substrate/layer interface; (b) EPMA profile of Yb^{3+} concentration across the interface.

interfacial roughness or crack propagation along the growth direction. The image was captured near the center of the sample, where the measured layer thickness was found to be 96.5 μm, in agreement with the average values obtained from optical microscopy.

In addition to the morphological evaluation, the dopant distribution near the interface was measured using EPMA. The compositional profile, shown in Figure 8(b), displays a sharp transition in Yb^{3+} concentration across the interface, with a clear separation between the undoped substrate and the doped epitaxial region. This abrupt change in Yb^{3+} content indicates minimal diffusion into the substrate, confirming effective dopant confinement during LPE growth and supporting the presence of a chemically and structurally distinct interface. Together, these results demonstrate the formation of a well-defined, high-quality epitaxial layer with excellent interface integrity, suitable for optical or functional applications where dopant localization is critical.

Figure 9 displays a photograph of an as-grown Tm^{3+}:$MgWO_4$ epitaxial layer on an $MgWO_4$ substrate. Approximately 7 mm of the substrate were immersed vertically into the solution, resulting in the formation of epitaxial layers on all faces of the dipped sample. The growth meniscus is clearly visible, marking the transition between immersed and nonimmersed regions. The resulting Tm-doped epitaxial layer is transparent and free of cracks, indicating good surface uniformity and minimal thermal stress accumulation during growth.

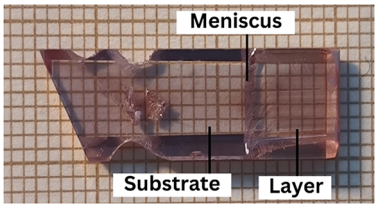

Figure 9. Photograph of the as-grown Tm^{3+}:$MgWO_4$ layer on the $MgWO_4$ substrate showing the (010) plane.

In comparison to the Yb^{3+}:$MgWO_4$ sample, which was grown under similar conditions but with a higher initial dopant concentration (20 at%) and slightly greater immersion depth (~9 mm), the Tm^{3+}-doped layer exhibits similarly good macroscopic coverage and surface quality. These morphological observations are consistent with the previously discussed structural results, which demonstrated lower lattice mismatch and a narrower rocking curve (FWHM) for the Tm^{3+} sample. Together, they confirm that the moderate Tm^{3+} doping level, combined with favorable lattice compatibility, supports the formation of a high-quality, uniform, and well-adhered epitaxial film.

The surface of the Tm^{3+}:$MgWO_4$ epitaxial layer, while generally smooth, is not perfectly flat. To quantitatively assess its morphology, a 3D surface topography was measured using a confocal optical microscope. A 2D transverse surface profile along the A−B direction was extracted from the topography

https://doi.org/10.1021/acs.cgd.5c00954
Cryst. Growth Des. 2025, 25, 9069−9077

scan, as shown in Figure 10. The rms roughness was determined to be 75.5 nm, indicating a highly smooth and uniform surface.

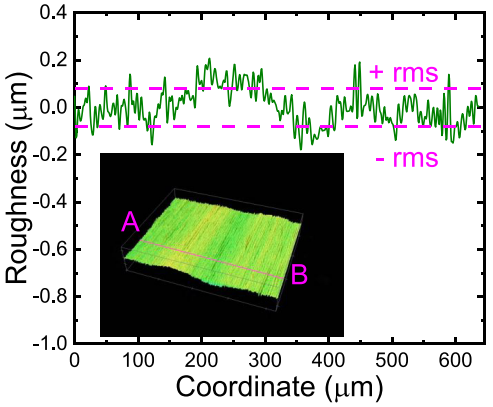

Figure 10. Surface roughness plot of the as-grown Tm^{3+}:$MgWO_4$ LPE layer: Dash lines indicate the range of root-mean-square (rms) deviation of the roughness, *inset*—the corresponding topography map, A-B *line*—the analyzed direction. Reflection mode, λ = 405 nm.

This value is more than eight times lower than that of the Yb^{3+}:$MgWO_4$ epitaxial layer (0.62 μm), reflecting a significant improvement in surface quality. The markedly smoother surface of the Tm^{3+}-doped sample may be attributed to the lower initial dopant concentration (10 at% Tm^{3+} vs 20 at% Yb^{3+}), which reduces the likelihood of dopant-induced surface instabilities, concentration, or interface strain during growth. The improved smoothness also aligns with the better crystalline quality and lower FWHM observed in the HRXRD analysis. We also note that faint growth lines were consistently observed on the Yb^{3+}:$MgWO_4$ layers, independent of the final layer thickness. These features are characteristic of step-flow growth under conditions of high concentration of doping elements in the solution. In contrast, such growth lines were absent in the Tm^{3+}:$MgWO_4$ films, consistent with their smoother morphology and lower initial dopant load. Overall, the combination of fine surface texture and structural integrity confirms the effectiveness of the growth conditions used for the Tm^{3+}:$MgWO_4$ epitaxial layer and further highlights the influence of dopant concentration and substrate quality on the morphological quality of the LPE-grown films.

To evaluate the substrate/layer interface and the dopant distribution within the Tm:$MgWO_4$ epitaxial layer, a lateral facet of the crystal was polished and inspected by ESEM in backscattered electron mode. As shown in Figure 11, the backscattered image reveals a well-defined, flat, and continuous interface between the epitaxial layer and the $MgWO_4$ substrate, with no visible delamination, roughness, or interfacial diffusion contrast. The thickness of the epitaxial layer was measured to be 300 ± 3 μm, indicating uniform growth across the substrate surface under the applied LPE conditions.

In addition to morphological assessment, the local concentration of Tm^{3+} ions was measured near the interface using quantitative EPMA. The resulting compositional profile shows a sharp transition in Tm content at the interface, confirming that the dopant remained confined to the epitaxial layer with negligible diffusion into the substrate. This abrupt interface reflects the limited diffusion of dopant ions, likely governed by the crystal structure and growth conditions, and is essential for preserving the optical and structural integrity of the film.

When compared to the Yb^{3+}:$MgWO_4$ sample, which showed a thinner layer (~96.5 μm) and a similarly sharp compositional boundary, the Tm^{3+}:$MgWO_4$ layer demonstrates both greater thickness and equally effective dopant confinement. These results are consistent with the lower lattice mismatch and improved crystalline quality discussed earlier, reinforcing the strong influence of dopant level and lattice compatibility on the final film morphology and interface sharpness.

4. CONCLUSION

In this study, we have successfully demonstrated the potential of Liquid Phase Epitaxy (LPE) for the growth of Tm^{3+}—and Yb^{3+}-doped single-crystalline $MgWO_4$ layers on undoped (010) oriented $MgWO_4$ substrates. Epitaxial films with thicknesses of up to several hundred micrometers were obtained, marking, to our knowledge, the first report of such epitaxial growth for this material system. The resulting layers exhibit several desirable characteristics: (i) a high-quality single-crystalline structure that is free of cracks and impurities, with a clean and well-defined interface between the layer and substrate; (ii) a well-preserved crystallographic orientation aligned with the substrate's [010] direction; (iii) minimal lattice mismatch with the substrate, ensuring strong compatibility between film and substrate. Detailed structural and

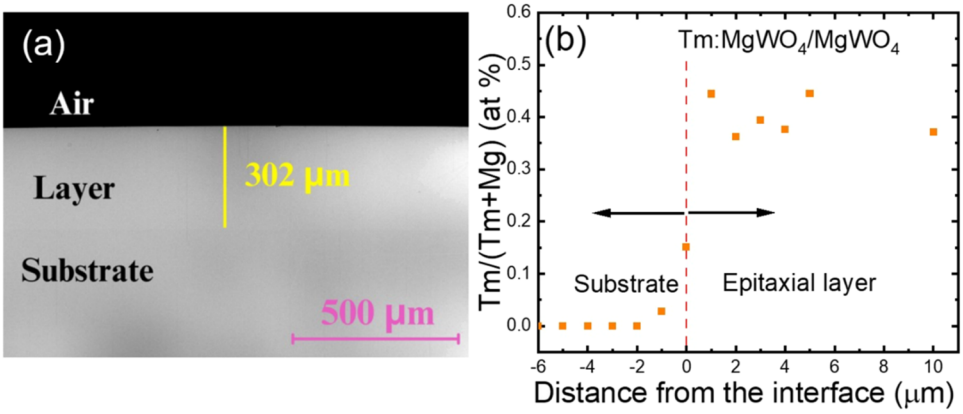

Figure 11. (a) Backscattered ESEM image of the polished edge of the Tm:$MgWO_4$/$MgWO_4$ epitaxy showing the substrate/layer interface; (b) EPMA profile of Tm^{3+} concentration across the interface.

https://doi.org/10.1021/acs.cgd.5c00954
Cryst. Growth Des. 2025, 25, 9069−9077

morphological analyses, including high-resolution X-ray diffraction, ESEM imaging, 3D surface profiling, and dopant distribution measurements, confirm the uniformity, structural integrity, and compositional sharpness of the grown layers. Notably, the Tm^{3+}-doped layers displayed a smoother surface and slightly superior crystal quality compared to their Yb^{3+}-doped counterparts, which is attributed to the lower dopant concentration and reduced lattice mismatch. Building on the well-established laser performance of Tm^{3+}- and Yb^{3+}-doped $MgWO_4$ bulk crystals and their favorable anisotropic properties, we anticipate that these high-quality epitaxial films will serve as promising candidates for thin-disk laser architectures. Their structural quality, broadband rare-earth emission potential, and scalability support their future integration into both continuous-wave and pulsed solid-state laser systems.

Considering the absorption cross-section obtained from bulk measurements, Yb^{3+}:$MgWO_4$ exhibits sufficiently high absorption (~10% per 100 μm for E ∥ N_g polarization), enabling the use of ~250 μm-thick epitaxial layers in thin-disk laser configuration to have good absorption efficiency by using a 4-pass pump geometry (2 bounces of the pump, i.e., one single retroreflection of the nonabsorbed pump power to simplify the pump geometry compared to the commercial Yb:YAG thin-disks which use up to 72 pump passes to compensate for the low absorption).

AUTHOR INFORMATION

Corresponding Author

Xavier Mateos − *Universitat Rovira i Virgili (URV), Física i Cristal·lografia de Materials (FiCMA), 43007 Tarragona, Spain;* Present Address: Serra Húnter Fellow, Serra 46118, Spain; orcid.org/0000-0003-1940-1990; Email: xavier.mateos@urv.cat

Authors

Ghassen Zin Elabedine − *Universitat Rovira i Virgili (URV), Física i Cristal·lografia de Materials (FiCMA), 43007 Tarragona, Spain;* orcid.org/0000-0002-6597-2439

Rosa Maria Solé − *Universitat Rovira i Virgili (URV), Física i Cristal·lografia de Materials (FiCMA), 43007 Tarragona, Spain;* orcid.org/0000-0002-5769-4141

Magdalena Aguiló − *Universitat Rovira i Virgili (URV), Física i Cristal·lografia de Materials (FiCMA), 43007 Tarragona, Spain*

Francesc Díaz − *Universitat Rovira i Virgili (URV), Física i Cristal·lografia de Materials (FiCMA), 43007 Tarragona, Spain*

Weidong Chen − *Max Born Institute for Nonlinear Optics and Short Pulse Spectroscopy, 12489 Berlin, Germany; Fujian Institute of Research on the Structure of Matter, Chinese Academy of Sciences, Fuzhou 350002 Fujian, China*

Valentin Petrov − *Max Born Institute for Nonlinear Optics and Short Pulse Spectroscopy, 12489 Berlin, Germany;* orcid.org/0000-0001-7247-6145

Complete contact information is available at: https://pubs.acs.org/10.1021/acs.cgd.5c00954

Notes

The authors declare no competing financial interest.

ACKNOWLEDGMENTS

Project PID2022-141499OB-100, funded by MICIU/AEI/10.13039/501100011033/and by FEDER/UE.

REFERENCES

(1) Ferrand, B.; Chambaz, B.; Couchaud, M. Liquid phase epitaxy: A versatile technique for the development of miniature optical components in single crystal dielectric media. *Opt. Mater.* **1999**, *11*, 101−114.

(2) Blank, S. L.; Nielsen, J. W. The growth of magnetic garnets by liquid phase epitaxy. *J. Cryst. Growth* **1972**, *17*, 302−311.

(3) Tien, P. K.; Martin, R. J.; Blank, S. L.; Wemple, S. H.; Varnerin, L. J. Optical waveguides of single-crystal garnet films. *Appl. Phys. Lett.* **1972**, *21*, 207−209.

(4) Aznar, A.; Silvestre, O.; Pujol, M. C.; Solé, R.; Aguiló, M.; Díaz, F. Liquid-phase epitaxy crystal growth of monoclinic $KLu_{1-x}Yb_x(WO_4)_2/KLu(WO_4)_2$ layers. *Cryst. Growth Des.* **2006**, *6*, 1781−1787.

(5) Gualtieri, D. M. Liquid phase epitaxy of yttrium aluminum garnet: Reduction of growth rate by germanium oxide. *Appl. Phys. Lett.* **1991**, *59*, 650−652.

(6) Starecki, F.; Bolaños, W.; Brasse, G.; Benayad, A.; Morales, M.; Doualan, J. L.; Braud, A.; Moncorgé, R.; Camy, P. Rare earth doped $LiYF_4$ single crystalline films grown by liquid phase epitaxy for the fabrication of planar waveguide lasers. *J. Cryst. Growth* **2014**, *401*, 537−541.

(7) Bolaños, W.; Carvajal, J. J.; Mateos, X.; Cantelar, E.; Lifante, G.; Griebner, U.; Petrov, V.; Panyutin, V. L.; Murugan, G. S.; Wilkinson, J. S.; Aguiló, M.; Díaz, F. Continuous-wave and Q-switched Tm-doped $KY(WO_4)_2$ planar waveguide laser at 1.84 μm. *Opt. Express* **2011**, *19*, 1449−1454.

(8) Sarnecki, J.; Podniesiński, D.; Nakielska, M. Epitaxial Nd^{3+}:YAG/YAG waveguide laser. *Opt. Mater. Express* **2022**, *12*, 3894−3903.

(9) Mateos, X.; Lamrini, S.; Scholle, K.; Fuhrberg, P.; Vatnik, S.; Loiko, P.; Vedin, I.; Aguiló, M.; Díaz, F.; Griebner, U.; Petrov, V. Holmium thin-disk laser based on $Ho:KY(WO_4)_2/KY(WO_4)_2$ epitaxy with 60% slope efficiency and simplified pump geometry. *Opt. Lett.* **2017**, *42*, 3490−3493.

(10) Rivier, S.; Mateos, X.; Silvestre, Ò.; Petrov, V.; Griebner, U.; Pujol, M. C.; Aguiló, M.; Díaz, F.; Vernay, S.; Rytz, D. Thin-disk $Yb:KLu(WO_4)_2$ laser with single-pass pumping. *Opt. Lett.* **2008**, *33*, 735−737.

(11) Vatnik, S.; Vedin, I.; Pujol, M. C.; Mateos, X.; Carvajal, J. J.; Aguilo, M.; Díaz, F.; Griebner, U.; Petrov, V. Thin disk Tm-laser based on highly doped $Tm:KLu(WO_4)_2/KLu(WO_4)_2$ epitaxy. *Laser Phys. Lett.* **2010**, *7*, 435−439.

(12) Zhang, L.; Huang, Y.; Sun, S.; Yuan, F.; Lin, Z.; Wang, G. Thermal and spectral characterization of Cr^{3+}:$MgWO_4$—a promising tunable laser material. *J. Lumin.* **2016**, *169*, 161−164.

(13) Loiko, P.; Chen, M.; Serres, J. M.; Aguiló, M.; Díaz, F.; Lin, H.; Zhang, G.; Zhang, L.; Lin, Z.; Camy, P.; Dai, S.-B.; Chen, Z.; Zhao, Y.; Wang, L.; Chen, W.; Griebner, U.; Petrov, V.; Mateos, X. Spectroscopy and high-power laser operation of a monoclinic Yb^{3+}:$MgWO_4$ crystal. *Opt. Lett.* **2020**, *45*, 1770−1773.

(14) Zhang, L.; Lin, H.; Zhang, G.; Mateos, X.; Maria, J. S.; Aguiló, M.; Díaz, F.; Griebner, U.; Petrov, V.; Wang, Y.; Loiko, P.; Vilejshikova, E.; Yumashev, K.; Lin, Z.; Chen, W. Crystal growth, optical spectroscopy and laser action of Tm^{3+}-doped monoclinic magnesium tungstate. *Opt. Express* **2017**, *25*, 3682−3693.

(15) Loiko, P.; Wang, Y.; Serres, J. M.; Mateos, X.; Aguiló, M.; Díaz, F.; Zhang, L.; Lin, Z.; Lin, H.; Zhang, G.; Vilejshikova, E.; Dunina, E.; Kornienko, A.; Fomicheva, L.; Petrov, V.; Griebner, U.; Chen, W. Monoclinic $Tm:MgWO_4$ crystal: Crystal-field analysis, tunable and vibronic laser demonstration. *J. Alloys Compd.* **2018**, *763*, 581−591.

(16) Loiko, P.; Serres, J. M.; Mateos, X.; Aguiló, M.; Díaz, F.; Zhang, L.; Lin, Z.; Lin, H.; Zhang, G.; Yumashev, K.; Petrov, V.; Griebner, U.; Wang, Y.; Choi, S. Y.; Rotermund, F.; Chen, W. Monoclinic Tm^{3+}:$MgWO_4$: a promising crystal for continuous-wave and passively Q-switched lasers at ~2 μm. *Opt. Lett.* **2017**, *42*, 1177−1180.

(17) Wang, Y.; Chen, W.; Mero, M.; Zhang, L.; Lin, H.; Lin, Z.; Zhang, G.; Rotermund, F.; Cho, Y. J.; Loiko, P.; Mateos, X.; Griebner,

U.; Petrov, V. Sub-100 fs Tm:$MgWO_4$ laser at 2017 nm mode locked by a graphene saturable absorber. *Opt. Lett.* **2017**, *42*, 3076−3079.
(18) Nie, H.-Y.; Lin, Z.-L.; Loiko, P.; Zeng, H.-J.; Zhang, L.; Lin, Z.; Elabedine, Zin.; Mateos, G.; Petrov, X.; Zhang, V.; Zhang, G.; Chen, W. Diode-pumped Kerr-lens mode-locked Yb:$MgWO_4$ laser. *Opt. Lett.* **2025**, *50*, 1049−1052.
(19) Elabedine, G. Z.; Solé, R. M.; Slimi, S.; Aguiló, M.; Díaz, F.; Chen, W.; Petrov, V.; Mateos, X. Growth, anisotropy, and spectroscopy of Tm^{3+} and Yb^{3+} doped $MgWO_4$ crystals. *CrystEngComm* **2025**, *27*, 1619−1631.
(20) Solé, R.; Nikolov, V.; Vilalta, A.; Carvajal, J. J.; Massons, J.; Gavaldà, J.; Aguiló, M.; Díaz, F. Liquid phase epitaxy of $KTiOPO_4$ on $KTi_{1-x}Ge_xOPO_4$ substrates. *J. Cryst. Growth* **2002**, *237*−*239*, 602−607.
(21) Silvestre, O.; Aznar, A.; Solé, R.; Pujol, M. C.; Díaz, F.; Aguiló, M. Lattice mismatch and crystal growth of monoclinic $KY_{1-x}Yb_x(WO_4)_2/KY(WO_4)_2$ layers by liquid phase epitaxy. *J. Phys.: Condens. Matter* **2008**, *20*, No. 225004.
(22) Shannon, R. D.; Prewitt, C. T. Revised values of effective ionic radii. *Acta Cryst. B* **1970**, *26*, 1046−1048.

https://doi.org/10.1021/acs.cgd.5c00954
Cryst. Growth Des. 2025, 25, 9069−9077